molecules

MDPI

Article

Disproportionation of H_2O_2 Mediated by Diiron-Peroxo Complexes as Catalase Mimics

Dóra Lakk-Bogáth, Patrik Török, Flóra Viktória Csendes, Soma Keszei, Beatrix Gantner and József Kaizer *

Research Group of Bioorganic and Biocoordination Chemistry, University of Pannonia, H-8201 Veszprém, Hungary; lakkd@almos.uni-pannon.hu (D.L.-B.); patriktrk6@gmail.com (P.T.); csvflora@gmail.com (F.V.C.); kornflakes09@gmail.com (S.K.); gantnerbea@gmail.com (B.G.)

* Correspondence: kaizer@almos.uni-pannon.hu; Tel.: +36-88-62-4720

Abstract: Heme iron and nonheme dimanganese catalases protect biological systems against oxidative damage caused by hydrogen peroxide. Rubrerythrins are ferritine-like nonheme diiron proteins, which are structurally and mechanistically distinct from the heme-type catalase but similar to a dimanganese KatB enzyme. In order to gain more insight into the mechanism of this curious enzyme reaction, non-heme structural and functional models were carried out by the use of mononuclear $[Fe^{II}(L_{1-4})(solvent)_3](ClO_4)_2$ (**1**–**4**) (L_1 = 1,3-bis(2-pyridyl-imino)isoindoline, L_2 = 1,3-bis(4′-methyl-2-pyridyl-imino)isoindoline, L_3 = 1,3-bis(4′-Chloro-2-pyridyl-imino)isoindoline, L_4 = 1,3-bis(5′-chloro-2-pyridyl-imino)isoindoline) complexes as catalysts, where the possible reactive intermediates, diiron-perroxo $[Fe^{III}{}_2(\mu\text{-}O)(\mu\text{-}1,2\text{-}O_2)(L_1\text{-}L_4)_2(Solv)_2]^{2+}$ (**5**–**8**) complexes are known and well-characterized. All the complexes displayed catalase-like activity, which provided clear evidence for the formation of diiron-peroxo species during the catalytic cycle. We also found that the fine-tuning of iron redox states is a critical issue, both the formation rate and the reactivity of the diiron-peroxo species showed linear correlation with the Fe^{III}/Fe^{II} redox potentials. Their stability and reactivity towards H_2O_2 was also investigated and based on kinetic and mechanistic studies a plausible mechanism, including a rate-determining hydrogen atom transfer between the H_2O_2 and diiron-peroxo species, was proposed. The present results provide one of the first examples of a nonheme diiron-peroxo complex, which shows a catalase-like reaction.

Keywords: catalase mimics; peroxide; diiron-peroxo complexes; structure/activity; kinetic studies

Citation: Lakk-Bogáth, D.; Török, P.; Csendes, F.V.; Keszei, S.; Gantner, B.; Kaizer, J. Disproportionation of H_2O_2 Mediated by Diiron-Peroxo Complexes as Catalase Mimics. *Molecules* **2021**, *26*, 4501. https://doi.org/10.3390/molecules26154501

Academic Editor: Chryssostomos Chatgilialoglu

Received: 7 July 2021
Accepted: 24 July 2021
Published: 26 July 2021

1. Introduction

Nonheme manganese catalases (MnCAT), as alternatives to the heme-containing catalases, contain a binuclear active sites and deplete hydrogen peroxide in cells through a ping-pong mechanism interconventing between Mn_2(II,II) and Mn_2(III,III) states in a two-electron catalytic cycle [1,2]. Manganese catalase enzymes such as *Lactobacillus plantarum* (LPC) [3,4], *Thermus thermophilus* (TTC) [5,6], *Thermoleophilium album* (TAC) [7], and *Pyrobaculum calidifontis VA1* (PCC) [8] have been isolated and characterized from both bacteria and archae. Despite their large numbers and importance, few catalase enzyme structures are known and they can also be sub-divided into two groups, each with a different active site.

Among them both LPC and TTC have a dimanganese catalytic core with Glu_3His_2 ligands coupled by two single-atom solvent bridges (Scheme 1A) [4,9]. In contrast to the above structure, the cyanobacterial manganese catalase (KatB) from *Anabaena* shows a markedly different active site with canonical Glu_4His_2 coordination geometry and two terminal water molecules (Scheme 1B). However, it closely resembles the active site of the ferritin-like ruberythrin (RBR), which is a nonheme diiron protein [10]. The Mn-Mn distances (~3.8 Å) in KatB are similar to that was observed for the iron-containing ribonucleotide reductase R2 (3.6–3.7 Å), but much shorter distances have been found for LPC and TTC (3.0–3.1 Å). The H_2O_2 binds terminally to one of the Mn center in LPC/TTC, while in

KatB and RBR, the symmetrical active sites and the relatively long M-M distances favor its μ-1,2 binding mode [11]. These enzymes, coupled with superoxide dimutates (SOD), are responsible for the full detoxification of $O_2^{\bullet-}$ through the formation of H_2O_2 and its redox disproportionation into water and dioxygen. H_2O_2 can also be classified as a ROS particle, since it readily reacts with reduced transition metals and results in highly reactive $HO^{\bullet}$ radical via Fenton-like reactions. Many rationally designed synthetic biomimetics are being developed against oxidative stress to treat various diseases, including Alzheimer's, cancer, aging, neurodegenerative, inflammatory and heart diseases [12–21]. The identification and study of the structure of the above enzymes can greatly contribute to the design of new catalase mimetics for potential therapeutic use. The structural and functional investigations on low molecular-weight copper, manganese and iron containing model compounds that are focused mainly on the effect of the used metals and their ligand environment (donor sites) on redox potential and through it on reactivity. Based on the literature data, various Schiff base, aminopyridine and azamacrocyclic derivatives have proven to be the most popular and practical ligands [12–21]. Considering the reactivity of manganese catalases (KatB) toward H_2O_2, including a ping-pong mechanism interconventing between Mn_2(II,II) and Mn_2(III,III) states in a two-electron catalytic cycle, a similar interaction with H_2O_2 has not been reported for diiron(III) peroxo intermediates which may be proposed in the catalytic cycles of RBR. Progress in recent years has made a number of diiron(III)-peroxo complexes available that can be generated by stoichiometric amount of H_2O_2 [22–27]. Therefore, the opportunity has arisen to investigate both electrophilic and nucleophilic reactivity towards various substrates, such as phenols, *N*,*N*-dimethylanilines, and various aldehydes, respectively [25,26]. The differences in reactivity observed in the investigated systems, as well as the stability of the peroxo intermediates can in principle be explained by the disproportionation of H_2O_2 as a competing process. Clarification of the relationship between catalase-like activity and catalytic oxidation is an important factor in the design and development of high efficiency catalytic systems. In addition, the investigation of the metal-based disproportionation of H_2O_2 may help us to understand the nature of the catalytically active species present both, in the enzymatic and biomimetic systems. We have reported that the $[Fe^{II}(L_1)(solvent)_3](ClO_4)_2$ (**1**) is an efficient catalyst for the oxidation of thioanisoles and benzyl alcohols by the use of H_2O_2 as cooxidant, where a metastabile green species (**5**) with a Fe^{III}(μ-O)(μ-1,2-O_2)Fe^{III} core was observed and characterized by UV-Vis, EPR, rRaman, and X-ray absorption spectroscopic measurements [24]. The reactivity of **5** was also published both in nucleophilic (deformylation of aldehydes) and electrophilic (oxidation of phenols) reactions [27].

As a possible functional model of RBR, we recently investigated the reactivity of the peroxo adduct $[Fe_2(\mu\text{-}O_2)(MeBzim\text{-}Py)_4(CH_3CN)]^{4+}$ (MeBzim-Py = (2-(2′-pyridyl)-*N*-methylbenzimidazole) with H_2O_2 and found direct kinetic and computational evidence for the formation of low-spin oxoiron(IV) via dissociation process [22,23]. As a continuation of this tudy, the previously reported and fully characterized Fe^{III}_2(μ-O)(μ-1,2-O_2)$(IndH)_2(Solv)_2]^{2+}$ (IndH = L_1 = 1,3-bis(2-pyridyl-imino)-isoindolines) [24,25] and their substituted isoindolin-containing derivatives (L_2–L_4, **2**–**4**) were chosen as model compounds, in which the dissociation of the diiron(III) core can be ruled out due to the μ-oxo-bridge, and investigated its reactivity towards H_2O_2 to gain insight into the mechanism of RBR enzymes (Scheme 2).

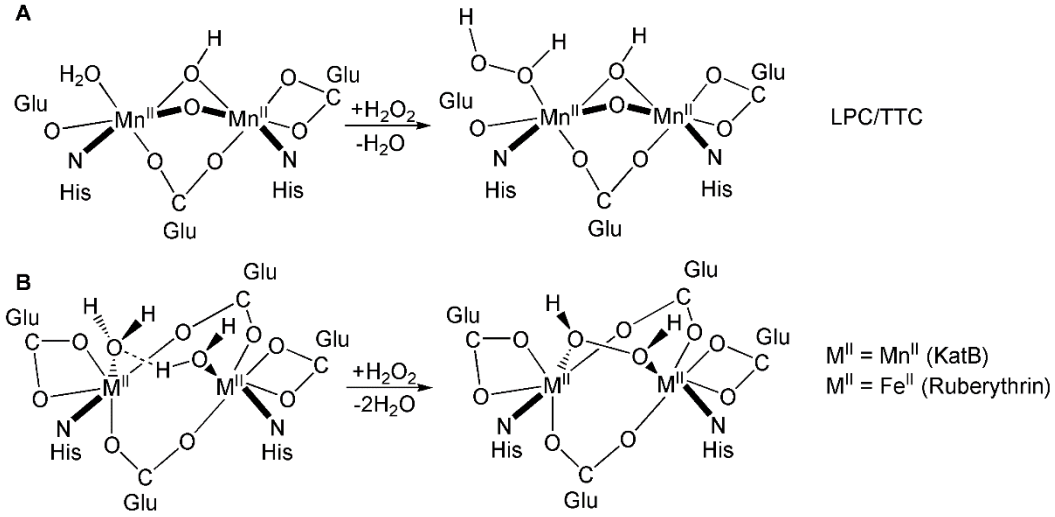

Scheme 1. Binding mode of H_2O_2 in nonheme dimanganese and diiron enzymes.

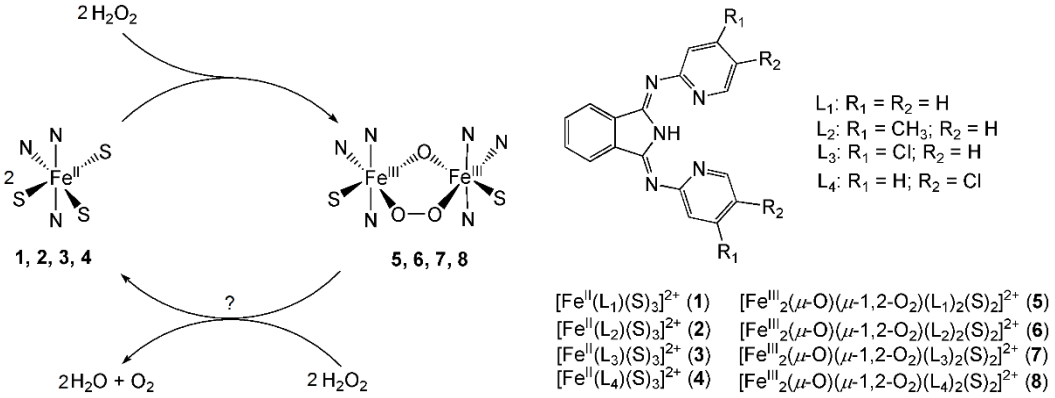

Scheme 2. Structural formulae for the ligands and their complexes used in the disproportionation reaction of H_2O_2.

2. Results and Discussions

In view of the above results, further studies were planned to elucidate the mechanism of both the diiron(III)-peroxo formation and its decay mediated by H_2O_2. Complex **5** from its precursor complex **1** can be generated even at room temperature by the use of excess of H_2O_2 in CH_3CN. Its formation and decay process was followed as an increase and decrease in absorbance at 690 nm (ε = 1500 M^{-1} cm^{-1} per Fe ion and assuming 100% conversion), which can be assigned as a charge transfer between Fe^{III} and the O_2^{2-} ligand (Figure 1a) [24]. Similar spectral feature can be observed for the complexes **6**–**8**: 691 nm (ε = 1404 M^{-1} cm^{-1}), 692 nm (ε = 1460 M^{-1} cm^{-1}), and 693 nm (ε = 1308 M^{-1} cm^{-1}), respectively. It is worth noting that the green species (**5**), after decomposition, can be regenerated 2–3 times by adding additional H_2O_2 without significant decrease on the yields (Table 1, Figure 1b and inset in Figure 2a). Similar behavior and yields were observed for **6**, but much lower values were obtained for **7** and **8**. These results are consistent with the stability and/or the reactivity of the intermediates at high concentrations of added water, providing further information for the possible role of the binding water during the formation of the reactive oxidant.

Preliminary kinetic studies were performed at 20 °C to establish the role of the observed diiron(III)-peroxo intermediates in the catalytic disproportionation reaction of H_2O_2. The formation and decomposition of **5** in the presence of H_2O_2 was monitored by following the rise and fall of its visible chromophore (Tables 2 and 3), as well as the appearance of the dioxygen formed by gas volumetric methods (Figure 2b). Dioxygen formation started

after a short lag phase during which the peroxo-adduct (**5**) accumulated. The lag phase was followed by a linear dioxygen formation period during which time **5** persisted in a pseudo-steady-state. This profile is similar to that found for the water-assisted decay of $Fe^{III}(H_2O)(OOH)$ intermediate into the reactive $Fe^{V}(O)(OH)$ species [28]. Upon depletion of H_2O_2, **5** decomposed rapidly and the dioxygen formation ceased. The yield of dioxygen, TON (turnover number = mol H_2O_2/mol catalyst) and the TOF (turnover frequency = mol H_2O_2/mol catalyst/h) values were determined to be Yield = 85%, TON = 10.4 and TOF = 288 h^{-1} as a result of volumetric method via the measurements of dioxygen evolution from the reaction mixture ($[H_2O_2]$ = 0.243 M and [**1**] = 0.002 M) at 20 °C in CH_3CN. Similar values were obtained for the complexes **2**, **3** and **4** under the same conditions (Table 4). The results clearly indicate that diiron-peroxo intermediates play a key role in the formation of the reactive species responsible for the H_2O_2 oxidation.

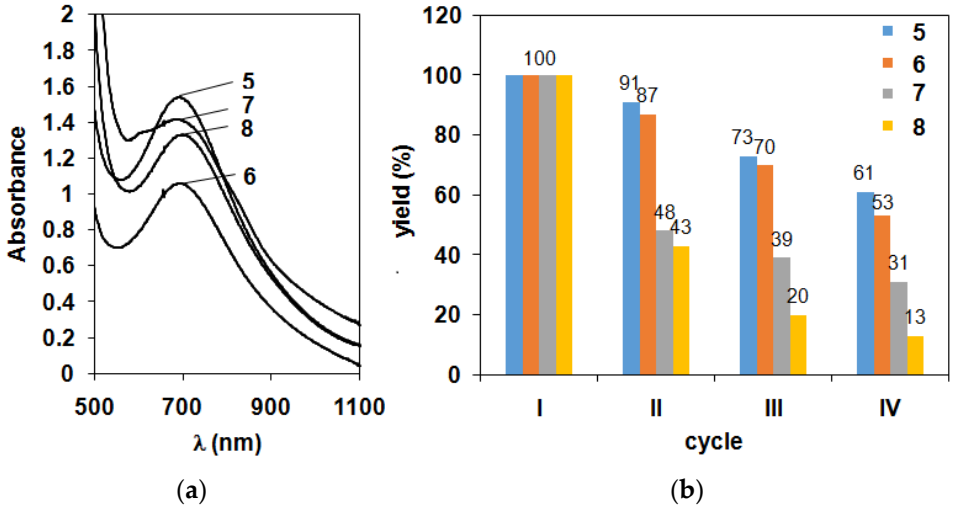

(**a**) (**b**)

Figure 1. (**a**) Characteristic UV-Vis spectra of $Fe^{III}_2(\mu\text{-}O)(\mu\text{-}1,2\text{-}O_2)(L_{1-4})_2(Solv)_2]^{2+}$ (**5**–**8**) intermediates in CH_3CN. (**b**) Dependence of the yield of peroxo complexes (**5**–**8**) on the number of cycles. $[Fe]_0$ = 2 mM, $[H_2O_2]_0$ = 24 mM (4x) in CH_3CN at 20 °C.

Table 1. Dependence of the yield of peroxo complexes (**5**–**8**) and the evolved oxygen (parantheses) on the number of cycles. $[Fe]_0$ = 2 mM, $[H_2O_2]_0$ = 24 mM (4×) in CH_3CN at 20 °C.

Cycles	Yield (5) and (O_2)/%	Yield (6)/%	Yield (7)/%	Yield (8)/%
I.	100 (95)	100	100	100
II.	91 (92)	87	48	43
III.	73 (78)	70	39	20
IV.	61 (64)	53	31	13
V.	41 (27)	36	26	12

2.1. Kinetic Studies on the Formation of Diiron-Peroxo Complexes (**5**–**8**)

Detailed kinetic studies on the reaction of **1** (2 mM) with H_2O_2 (24–98 mM) were carried out in CH_3CN at 15 °C, and the formation of the green species **5** was followed by UV-vis spectroscopy as an increase in absorbance at 690 nm under pseudo-first-order conditions (excess of H_2O_2) (Table 2). At constant $[\mathbf{1}]_0$ = 2 mM, the formation of **5** exhibits a first-order dependence, and the first-order rate constants show a good linear dependence with $[H_2O_2]_0$ (Figure 3a), affording the second-order rate constant k_2 = 0.93 M^{-1} s^{-1} at 15 °C and 1.09 M^{-1} s^{-1} at 20 °C. These values are about 5–6 times smaller than those obtained for $[Fe^{II}(MeBzim\text{-}Py)]^{2+}$ (5.5 M^{-1} s^{-1}), $Fe^{II}(MeBzim\text{-}Py)^{2+}$ (6.6 M^{-1} s^{-1}) and $Fe^{II}(TBA)^{2+}$ (6.54 M^{-1} s^{-1}) complexes under the same conditions at 20 °C [23,26]. It is worth noting that adding large volumes of water (~0.5 M) resulted in nearly twice the rate of the diiron-peroxo formation. Furthermore, a kinetic isotope effect (KIE) of 2.99 and 3.07

were observed for the formation of **6** and **7**, when the experiments were carried out in the presence of added H_2O or D_2O. This value may represent the result of much more multiple effects compared to the elemental step, but clearly indicate the key role of the water during the diiron-peroxo complex formation.

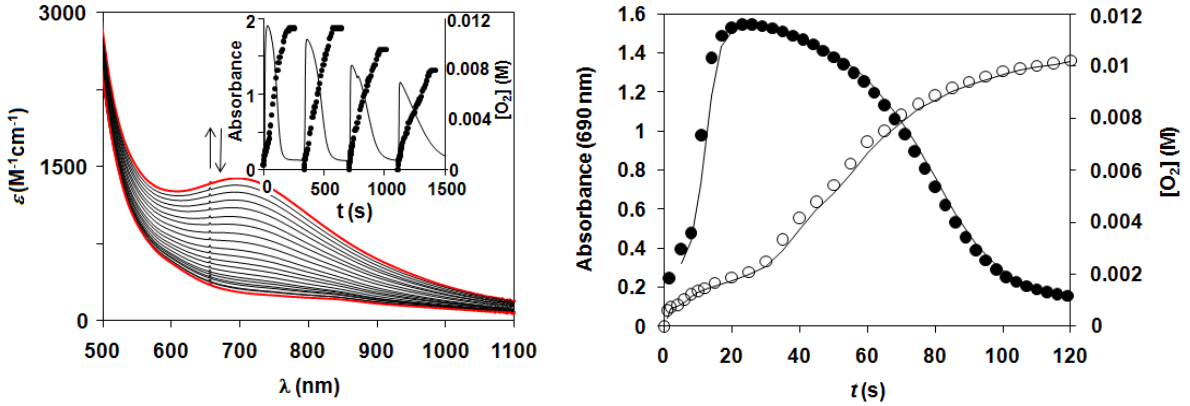

Figure 2. (**a**) UV-Vis spectral changes of **5** during the **1**-catalyzed disproportionation of H_2O_2. The inset shows the the time course of the formation and decay of **5** and the parallel formation of dioxygen for 5 cycles. $[\mathbf{5}]_0$ = 2 mM, $[H_2O_2]_0$ = 24 mM (4×) in CH_3CN at 20 °C (**b**) Time course for the H_2O_2 (24 mM) oxidation by **5** (2 mM), monitored at 690 nm in CH_3CN at 20 °C and by volumetrically determined amounts of evolved dioxygen.

Table 2. Kinetic data for the formation of intermediates **5**, **6**, **7** and **8** in CH_3CN.

Nr.	Complex	T/°C	$[\mathbf{1–4}]_0$/mM	$[H_2O_2]_0$/M	$k_{obs}10^{-2}$ s^{-1}	k_2/M^{-1} s^{-1}
1	**1**	15	2	0.0243	2.12	0.87 ± 0.03
2	**1**	15	2	0.0367	3.15	0.86 ± 0.04
3	**1**	15	2	0.0489	4.07	0.83 ± 0.03
4	**1**	15	2	0.0734	6.76	0.92 ± 0.04
5	**1**	15	2	0.0979	9.04	0.92 ± 0.03
6	**2**	15	2	0.0243	4.45	1.83 ± 0.09
7	**2**	15	2	0.0367	5.83	1.58 ± 0.05
8	**2**	15	2	0.0489	8.44	1.72 ± 0.06
9	**2**	15	2	0.0734	10.5	1.43 ± 0.04
10	**2**	15	2	0.0979	14.45	1.48 ± 0.04
11	**3**	15	2	0.0243	9.22	3.79 ± 0.15
12	**3**	15	2	0.0367	12.64	3.44 ± 0.13
13	**3**	15	2	0.0489	16.95	3.46 ± 0.14
14	**3**	15	2	0.0734	24.61	3.35 ± 0.14
15	**3**	15	2	0.0979	31.07	3.17 ± 0.11
16	**4**	15	2	0.0243	9.25	3.81 ± 0.15
17	**4**	15	2	0.0367	13.17	3.59 ± 0.14
18	**4**	15	2	0.0489	18.48	3.78 ± 0.16
19	**4**	15	2	0.0734	27.07	3.69 ± 0.15
20	**4**	15	2	0.0979	35.83	3.66 ± 0.15

Table 3. Kinetic data for the disproportionation of H_2O_2 mediated by **5**, **6**, **7** and **8** in CH_3CN.

Nr.	Complex	T/°C	$[1–4]_0$/mM	$[H_2O_2]_0$/M	$k_{obs}/10^{-3}$ s^{-1}	$k_2/10^{-2}$ M^{-1} s^{-1}
1	**1**	15	0.738	0.0243	0.358	1.47 ± 0.06
2	**1**	15	1.48	0.0243	0.387	1.59 ± 0.07
3	**1**	15	2	0.0243	0.370	1.52 ± 0.06
4	**1**	5	2	0.0243	0.116	0.477 ± 0.02
5	**1**	10	2	0.0243	0.160	0.658 ± 0.03
6	**1**	20	2	0.0243	0.523	2.15 ± 0.11
7	**1**	25	2	0.1	3.33	3.33 ± 0.11
8	**1**	25	2	0.2	5.57	2.79 ± 0.08
9	**1**	25	2	0.3	10.1	3.36 ± 0.09
10	**1**	25	2	0.6	17.3	2.89 ± 0.07
11	**1**	25	2	0.9	27.1	3.01 ± 0.06
12	**1**	25	0.3	0.3	10.3	3.42 ± 0.12
13	**1**	25	0.6	0.3	10.1	3.38 ± 0.11
14	**1**	25	1	0.3	11.1	3.68 ± 0.14
15	**1**	25	1.4	0.3	9.47	3.16 ± 0.13
16	**1**	10	2	0.3	1.99	0.663 ± 0.02
17	**1**	15	2	0.3	3.63	1.21 ± 0.05
18	**1**	20	2	0.3	6.12	2.04 ± 0.08
19	**2**	15	0.738	0.0243	0.823	3.39 ± 0.11
20	**2**	15	1.07	0.0243	0.692	2.85 ± 0.09
21	**2**	15	1.48	0.0243	0.772	3.18 ± 0.10
22	**2**	15	1.77	0.0243	0.744	3.06 ± 0.09
23	**2**	15	2	0.0243	0.730	3.00 ± 0.11
24	**2**	5	2	0.0243	0.332	1.37 ± 0.04
25	**2**	10	2	0.0243	0.413	1.70 ± 0.05
26	**2**	20	2	0.0243	1.09	4.49 ± 0.27
27	**3**	15	0.738	0.0243	3.92	16.1 ± 0.72
28	**3**	15	1.48	0.0243	4.71	19.4 ± 0.62
29	**3**	15	2	0.0243	4.83	19.9 ± 0.68
30	**3**	5	2	0.0243	2.42	9.96 ± 0.35
31	**3**	10	2	0.0243	3.41	14.01 ± 0.63
32	**3**	20	2	0.0243	8.90	36.6 ± 2.01
33	**4**	15	0.738	0.0243	5.49	22.6 ± 0.79
34	**4**	15	1.48	0.0243	5.44	22.4 ± 0.83
35	**4**	15	2	0.0243	5.75	23.8 ± 0.85
36	**4**	5	2	0.0243	2.89	11.9 ± 0.48
37	**4**	10	2	0.0243	4.20	17.3 ± 0.67
38	**4**	20	2	0.0243	10.2	42.01 ± 1.77

In the next step, we investigated the effect of the the ligand modification by introducing electron withdrawing (Cl) or electron releasing (CH_3) substituents on the pyridine arms in the fourth and fifth positions with emphasis on the redox potential and Lewis acidity of the precursor complex. Since the redox potential of the substituted complexes can be measured under the same conditions, it can be used as excellent reactivity descriptor. On the cyclic voltammogram of the Fe(II)-isoindoline complexes (**1**–**4**) irreversible reduction and oxidation peaks can be recognized within the range of −440 to +1160 mV (vs. Fc/Fc^+). The huge peak separations ($\Delta E = E_{pa} - E_{pc}$, Table 4) indicates the irreversibility of the redox processes and suggests chemical reactions coupled to the electrode reaction. The results, obtained at the scan rate of 100 mV/s, show that oxidation potential is mainly influenced by the electronic properties of the ligands, since the anodic peak potentials (E_{pa}) of the complexes are increasing in the order of electron releasing ability of the substituent on the pyridine moiety (Figure 4). The E_{pa} spans a 128 mV range from 655 mV (**1**) to 783 mV (**4**), which is not too large but informative, in terms of the effect of the substituents. However, the fact that the anodic peak of complex **1** can be found at lower potentials than it could be expected according to electronic effects, suggest that steric effects are also influencing the oxidation reactions. One can assume that the steric effect of the methylated and chlorinated ligands can cause an anodic shift in the oxidation peak potential of the complexes.

Table 4. Rate constants, electrochemical data and activation parameters for the formation of $Fe^{III}_2(\mu\text{-}O)(\mu\text{-}1,2\text{-}O_2)(L_1\text{-}L_4)_2(Solv)_2]^{2+}$ (**5–8**) complexes and their catalase-like reactions.

	1 (5)	2 (6)	3 (7)	4 (8)
$E_{pa}(Fe^{II}/Fe^{III})$/mV vs. Fc/Fc^+	655	683	765	783
$E_{pc}(Fe^{II}/Fe^{III})$/(mV vs. Fc/Fc^+	−90	−223	−155	−143
ΔE/mV	745	905	920	925
yield/%	85	100	92	85
TON ([S]/[Fe])	10.4	12.2	11.3	10.4
TOF ([S]/[Fe]/h)	288	418	354	234
k_2(cat)/10^{-2} M^{-1} s^{-1} (15 °C)	1.52	3.05	19.9	23.8
$E_{A/}$kJ mol^{-1}	72.3	55.9	57.5	55.5
$\Delta S^{\neq}$/J mol^{-1} K^{-1}	−37.7	−88.1	−65.9	−71.4
$\Delta H^{\neq}$/kJ mol^{-1}	70	53.5	55	53.1
$\Delta G^{\neq}$/kJ mol^{-1}	81	78.9	74	73.7
k_{decay}/$10^{-2}s^{-1}$ (15 °C)	0.13	0.15	1.22	1.41
k_{form}/M^{-1} s^{-1} (15 °C)	0.93	1.43	3.16	3.66

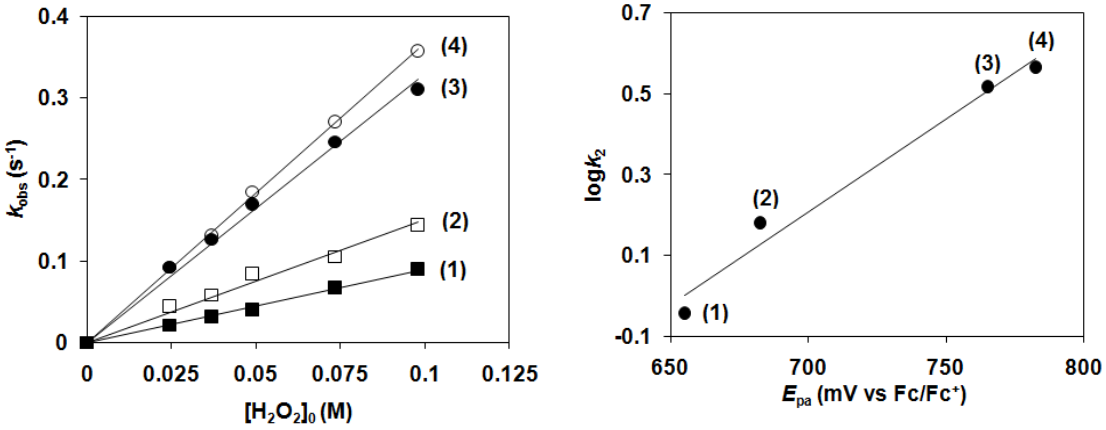

(**a**) (**b**)

Figure 3. (**a**) Formation of diiron-peroxo (**5–8**) complexes. Plots of k_{obs} against H_2O_2 concentration to determine a second-order rate constant. $[\mathbf{1–4}]_0$ = 2 mM, in CH_3CN at 15 °C. (**b**) Dependence of the formation rate of peroxo-diiron complexes (**5–8**) on the oxidation potential (E_{pa}) of the $[Fe^{II}(L_{1–4})(solvent)_3](ClO_4)_2$ (**1–4**) complexes.

The four iron complexes, **1–4** have been compared to investigate the effect of the various aryl substituents. Figure 3a shows the results of the activity for the precursor complexes (**1–4**) during the formation of their appropriate diiron-peroxo intermediates (**5–8**). This demonstrates only small differences exist, based on the first-order rate constants obtained under the same conditions. It was found that complex **4** with 5-chloropyridyl side chains is the most reactive complex with k_{obs} of 3.66 M^{-1} s^{-1}, whilst complex **1** with unsubstituted side chains was proved to be the least active with k_{obs} of 0.93 M^{-1} s^{-1} at 15 °C. Based on the CV data, we have got a clear evidence that the formation rate of the diiron-peroxo species (k_2) increases almost linearly with the redox potential (E_{pa} for Fe^{III}/Fe^{II}) of the precursor complex (Figure 3b). In summary, the higher the redox potentials of Fe^{III}/Fe^{II} redox couple the higher is the activity of the precursor complex towards to H_2O_2. Complexes with 4- and 5-chloro-pyridine side chains (**3** and **4**), whose metal sites are electron-deficient are faster in their reaction with H_2O_2 than electron-rich derivatives **1** and **2** with more Lewis basic side chains.

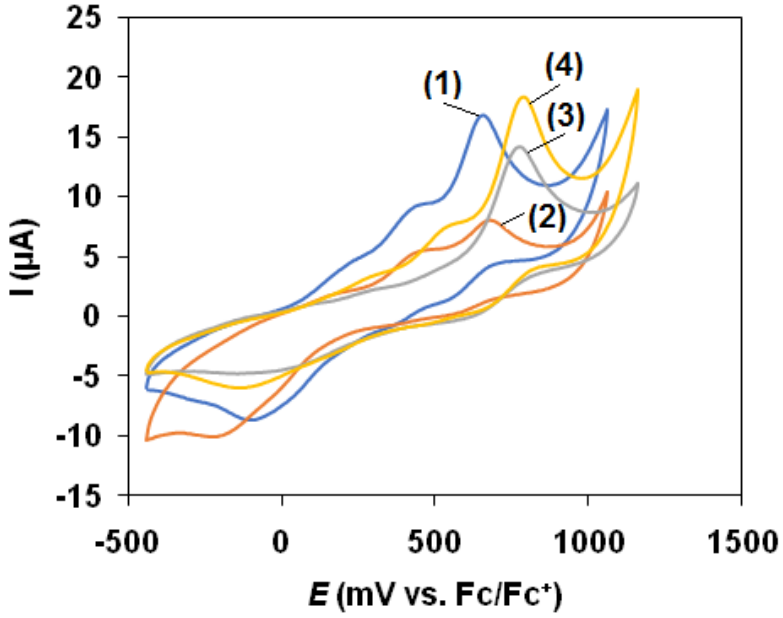

Figure 4. Cyclic voltammograms of $[Fe^{II}(L_{1–4})(solvent)_3](ClO_4)_2$ complexes (**1**–**4**) (5 mM in acetonitrile, supporting electrolyte: tetrabutylammonium-perchlorate (0.1 M), scan rate: 100 mV/s).

2.2. Catalase-Like Activity of Peroxo-Diiron Complexes

The ability of the in situ generated diiron-peroxo species (**5**) to mediate the disproportionation reaction of H_2O_2 into O_2 and H_2O was tested in CH_3CN by UV-vis spectroscopy as a decrease in absorbance at 690 nm under pseudo-first-order conditions (excess of H_2O_2) (Table 3). The initial rate of decay of diiron-peroxo species was measured as a function of the complex and substrate concentrations in CH_3CN. At constant $[H_2O_2]_0$ = 300 mM, the disproportionation reaction shows first-order kinetic behavior on [5], and the first-order rate constant $k_1 = 4.968 \times 10^{-3}$ s^{-1} was obtained at 20 °C from the slope of the plot of V_i versus $[\mathbf{5}]_0$ (Figure 5a). At constant $[\mathbf{5}]_0$ = 2 mM, initial rates (V_i) exhibit a linear dependence with $[H_2O_2]_0$ (Figure 5b) affording first-order rate constant $k_{1'} = 29.63 \times 10^{-3}$ s^{-1}. The second-order rate constant, $k_2 = 3.4$ M^{-1} s^{-1} was obtained from either $k_1/[H_2O_2]_0$ or $k_{1'}/[\mathbf{5}]_0$. This value is much smaller than that was found for the analogue $[Mn(L_1)]^{2+}$ complex ($k_2(k_{cat}/K_M) = 79 \pm 4$ M^{-1} s^{-1}) in protic solution, where $Mn^{IV}(O)$ intermediate was proposed as reactive species [29]. A kinetic isotope effect (KIE) of 1.73 and 1.66 were observed for the decay of **6** and **7**, when the experiments were carried out in the presence of added H_2O or D_2O. These results indicate the key role of the water during the diiron-peroxo mediated disproportionation reaction.

In the next step, we investigated the effect of the ligand modification by introducing electron donating (-CH_3) and electron withdrawing (-Cl) phenyl-ring substituents. The substituted ligand-containing diiron-peroxo intermediates **5**, **6**, **7** and **8** show an increasing rate in the listed order (Figure 6a). It was found that complex **8** with 5-chloropyridine side chains is the most efficient oxidant with the fastest rate $k_2 = 23.8 \times 10^{-2}$ M^{-1} s^{-1}, while complexes **5** and **6** with unsubstituted and 4-methylpyridine side chains are the less efficient oxidants with $k_2 = 1.52 \times 10^{-2}$ M^{-1} s^{-1} and $k_2 = 3.05 \times 10^{-2}$ M^{-1} s^{-1}, respectively. These results give clear evidence that substituents affect the redox potential and the catalase activity of the complexes. Table 4 and Figure 6b show that the redox potentials (E_{pa}) of the complexes and their activity increase with increasing electron-withdrawing ability of the substituent.

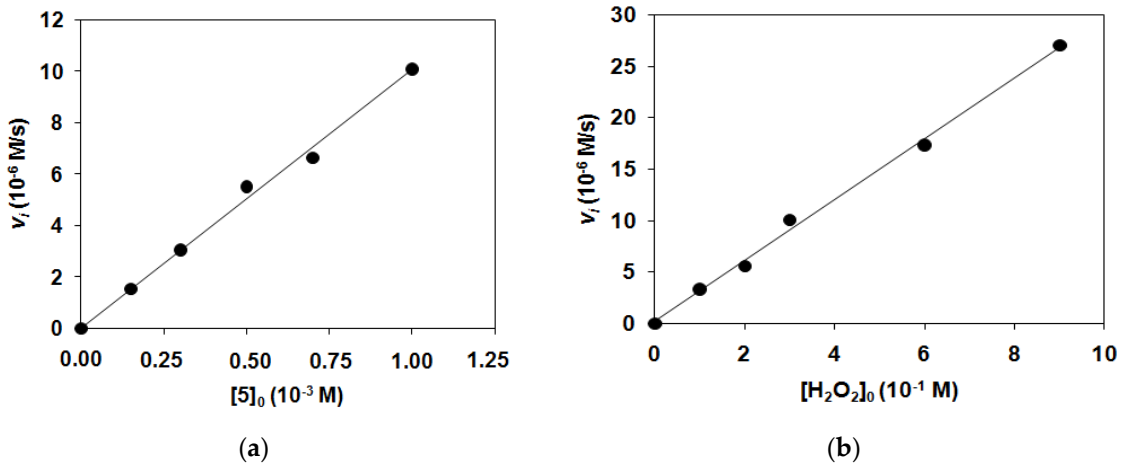

(**a**) (**b**)

Figure 5. **5**-mediated disproportionation of H_2O_2 in CH_3CN at 25 °C. (**a**) Dependence of the reaction rate (V_i) for H_2O_2 oxidation on the diiron-peroxo complex **5** concentration. [H_2O_2]$_0$ = 300 mM (**b**) Dependence of the reaction rate (V_i) for H_2O_2 oxidation on the H_2O_2 concentration. [**5**]$_0$ = 1 mM.

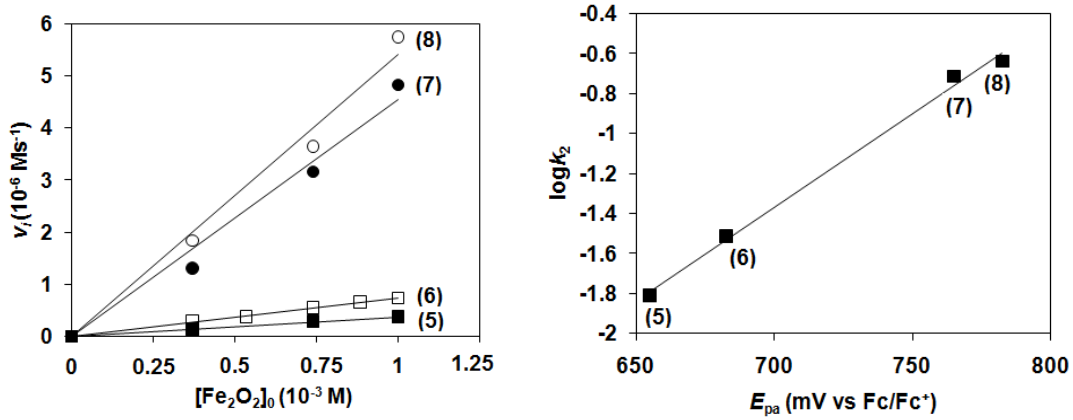

(**a**) (**b**)

Figure 6. Peroxo-diiron complexes-mediated disproportionation of H_2O_2 in CH_3CN at 15 °C. (**a**) Dependence of the reaction rate (V_i) for H_2O_2 oxidation on the diiron-peroxo complex **5**–**8** concentration. [H_2O_2]$_0$ = 24 mM (**b**) Dependence of the decay rate of peroxo-diiron complexes (**5**–**8**) on the oxidation potential (E_{pa}) of the [$Fe^{II}(L_{1–4})(solvent)_3$]$(ClO_4)_2$ (**1**–**4**) complexes.

Based on the temperature dependence of the reactivity of diiron-peroxo complexes (Figure 7a), the experimentally determined the difference between $\Delta G^{\neq}$ values was 7.3 kJ mol^{-1}. Significantly lower free activation energy value was obtained for the **8**-mediated disproportionation of H_2O_2 in comparison to **5**. The calculated Gibbs energy values correlate very well with the reaction rates (Figure 7b). The values of $-T\Delta S^{\neq}$ were lower than $\Delta H^{\neq}$ in the investigated temperature range, indicating an enthalpy-controlled reactions. As a result of a compensation effect increasing activation enthalpies are offset by increasingly poitive entropies yielding $\Delta H^{\neq}$ = 81 kJ mol^{-1} at the intercept (Figure 8), which value is a little bit higher than that was obtained for the conversion alkylperoxo-iron(III) intermediates to oxoiron(IV) through O-O bond homolysis ($\Delta H^{\neq}$ = 61.3 kJ mol^{-1}) [30].

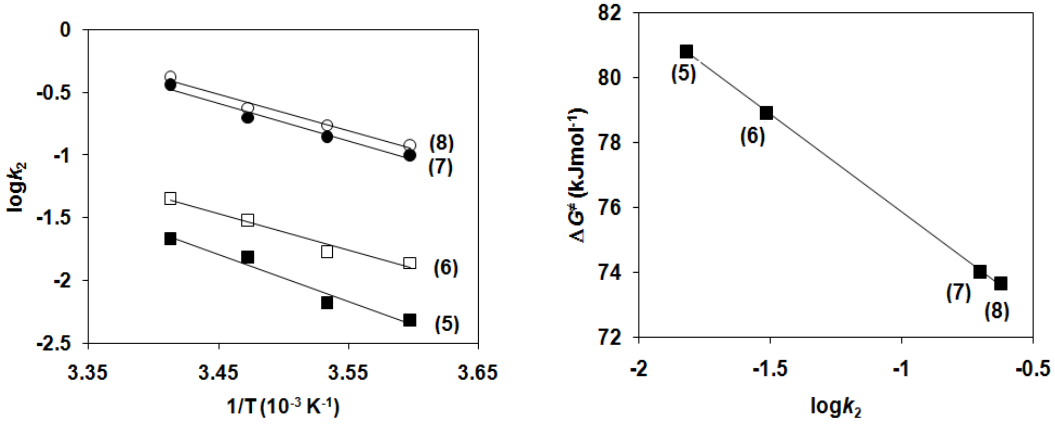

(**a**) (**b**)

Figure 7. (**a**) Arrhenius plots of logk_2 versus 1/T for the Fe^{III}_2(μ-O)(μ-1,2-O_2)($L_{1–4}$)$_2$(Solv)$_2$]$^{2+}$ (**5**–**8**)-mediated disproportionation of H_2O_2 in CH_3CN. [**5**–**8**]$_0$ = 2 mM, [H_2O_2]$_0$ = 24 mM. (**b**) Plot of $\Delta G^{\neq}$ versus lgk_2 for the reaction of [Fe^{III}_2(μ-O)(μ-1,2-O_2)($L_{1–4}$)$_2$(Solv)$_2$]$^{2+}$ (**5**–**8**) with H_2O_2.

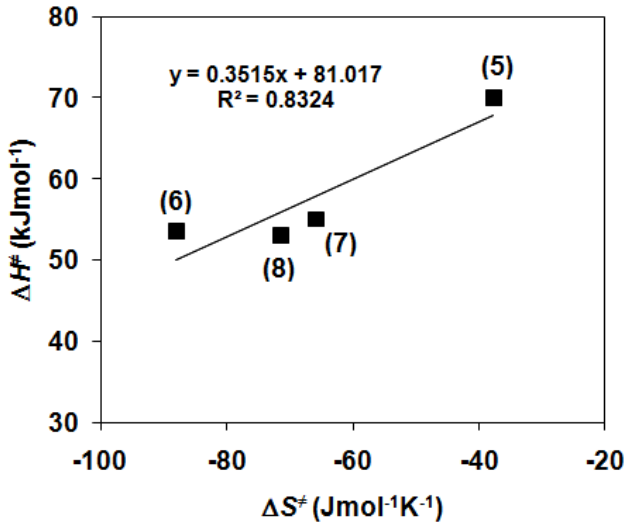

Figure 8. Isokinetic plot for the for the Fe^{III}_2(μ-O)(μ-1,2-O_2)($L_{1–4}$)$_2$(Solv)$_2$]$^{2+}$ (**5**–**8**)-mediated disproportionation of H_2O_2 in CH_3CN.

3. Experimental

3.1. Materials and Methods

The ligands 1,3-bis(2′-pyridylimino)isoindolines (L_1 = indH, L_2 = 4Me-indH, L_3 = 4Cl-indH, L_4 = 5Cl-indH,) and their complexes (**1**–**4**) were prepared according to published procedures [31]. All manipulations were performed under a pure argon atmosphere using standard Schlenk-type inert-gas techniques. Solvents used for the reactions were purified by literature methods and stored under argon. The starting materials for the ligand are commercially available and they were purchased from Sigma Aldrich. The UV-visible spectra were recorded on an Agilent 8453 diode-array spectrophotometer using quartz cells. IR spectra were recorded using a Thermo Nicolet Avatar 330 FT-IR instrument (Thermo Nicolet Corporation, Madison, WI, USA), Samples were prepared in the form of KBr pellets. Microanalyses elemental analysis was done by the Microanalytical Service of the University of Pannonia.

3.2. Characterization of Ligands and Their Complexes

indH: FT-IR (ATR) ν = 3199 (w), 3061 (w), 1622 (s), 1606 (m), 1577 (s), 1550 (s), 1454 (s), 1427 (s), 1373 (m), 1306 (m), 1259 (s), 1217 (s), 1139 (m), 1097 (m), 1042 (m), 991 (w), 885 (w),

875 (w), 859 (w), 839 (w), 808 (m), 792 (s), 783 (s), 769 (s), 737 (s), 708 (m), 696 (s), 689 (s), 627 (w). UV/Vis (DMF): λ_{max} (logε) = 317 (3.09), 332 (3.18), 348 (3.21), 368 (3.28), 386 (3.34), 410 (3.11) nm.

4Me-ind: FT-IR (ATR) ν = 3209 (w), 3049 (w), 1645 (m), 1627 (s), 1591 (s), 1541 (m), 1460 (s), 1408 (w), 1364 (m), 1305 (m), 1281 (m), 1242 (s), 1186 (m), 1132 (w), 1114 (w), 1101 (m), 1036 (m), 997 (w), 929 (m), 891 (m), 848 (w), 810 (s), 779 (m), 742 (w), 694 (s), 660 (w). UV/Vis (DMF): λ_{max} (logε) = 316 (2.99), 332 (3.08), 348 (3.12), 366 (3.18), 387 (3.21), 411 (2.98) nm.

4Cl-ind: FT-IR (ATR) ν = 3213 (w), 1743 (w), 1637 (m), 1624 (m), 1565 (s), 1539 (m), 1448 (s), 1359 (m), 1309 (m), 1300 (m), 1281 (w), 1219 (m), 1184 (w), 1089 (m), 1040 (m), 989 (m), 895 (s), 877 (s), 804 (m), 779 (m), 735 (s), 701 (s) 687 (m), 656 (w). UV/Vis (DMF): λ_{max} (logε) = 315 (3.16), 332 (3.27), 348 (3.29), 367 (3.31), 385 (3.35), 409 (3.12) nm.

5Cl-ind: FT-IR (ATR) ν = 3317 (w), 3228 (w), 1745 (m), 1633 (s), 1572 (s), 1470 (m), 1447 (s), 1359 (m), 1311 (m), 1256 (w), 1244 (w), 1228 (m), 1217 (m), 1184 (w), 1105 (s), 1034 (s), 1007 (m), 955 (w), 924 (w), 880 (w), 843 (s), 773 (s), 754 (m), 725 (w), 702 (s), 691 (s), 638 (m), 619 (w), 602 (m). UV/Vis (DMF): λ_{max} (logε) = 338 (3.15), 354 (3.15), 376 (3.19), 395 (3.25), 421 (3.02) nm.

1: FT-IR (ATR) ν = 3329 (w), 1728 (w), 1654 (m), 1626 (s), 1614 (m), 1593 (w), 1554 (w), 1524 (s), 1485 (s), 1467 (m), 1433 (m), 1373 (w), 1304 (w), 1262 (w), 1207 (m), 1055 (s), 929 (w), 860 (w), 779 (s), 714 (m), 621 (m). $C_{24}H_{20}Cl_2FeN_8O_8$ (675.22): calcd. C 42.69, H 2.99, Cl 10.15, N 16.60; found C 42.82, H 2.93, Cl 10.11, N 16.42. UV/Vis (CH_3CN): λ_{max} (logε) = 315 (3.36), 329 (3.45), 345 (3.48), 365 (3.56), 382 (3.61), 406 (3.37) nm.

2: FT-IR (ATR) ν = 3456 (w), 1734 (w), 1665 (m), 1654 (s), 1605 (s), 1551 (m), 1520 (s), 1493 (s), 1477 (m), 1367 (w), 1313 (w), 1279 (m), 1244 (w), 1215 (w), 1049 (s), 941 (w), 827 (w), 777 (w), 752 (w), 710 (m), 621 (m). $C_{26}H_{27}Cl_2FeN_8O_8$ (706.29): calcd. C 44.21, H 3.85, Cl 10.04, N 15.87; found C 43.99, H 3.64, Cl 9.58, N 15.79. UV/Vis (CH_3CN): λ_{max} (logε) = 315 (3.48), 328 (3.58), 345 (3.62), 365 (3.71), 383 (3.76), 406 (3.50) nm.

3: FT-IR (ATR) ν = 3366 (w), 3217 (w), 1773 (w), 1724 (w), 1670(m), 1628 (m), 1564 (m), 1543 (m), 1516 (s), 1483 (m), 1460 (s), 1362 (w), 1306 (w), 1228 (w), 1205 (m), 1090 (s), 1051 (s), 910 (m), 867 (w), 823 (w), 744 (s), 710 (s), 621 (m). $C_{24}H_{21}Cl_4FeN_8O_8$ (747.13): calcd. C 38.58, H 2.83, Cl 18.98, N 15.00; found C 38.25, H 2.95, Cl 18.63, N 15.52. UV/Vis (CH_3CN): λ_{max} (logε) = 328 (3.10), 344 (3.09), 363 (3.04), 383 (2.99), 406 (2.71) nm.

4: FT-IR (ATR) ν = 3323 (w), 3228 (w), 1773 (w), 1717 (w), 1651(w), 1628 (m), 1612 (m), 1546 (m), 1521 (s), 1477 (s), 1458 (s), 1391 (w), 1366 (m), 1335 (w), 1298 (w), 1261 (w), 1236 (m), 1205 (m), 1096 (s), 1076 (s), 922 (m), 851 (w), 835 (m), 781 (w), 752 (m), 711 (s), 650 (w), 621 (m). $C_{24}H_{21}Cl_4FeN_8O_8$ (747.13): calcd. C 38.58, H 2.83, Cl 18.98, N 15.00; found C 38.81, H 3.04, Cl 18.63, N 15.39. UV/Vis (CH_3CN): λ_{max} (logε) = 335 (2.64), 353 (2.59), 373 (2.47), 395 (2.36), 418 (2.04) nm.

3.3. Cyclic Voltammetry

Cyclic voltammetry experiments were performed on a Radiometer Analytical PGZ-301 potentiostat with a conventional three-electrode configuration, consisting of a glassy carbon working electrode (ID = 3 mm), a platinum wire auxiliary electrode, and Ag/AgCl reference electrode. Potentials are referenced to the Fc/Fc^+ redox couple. Ferrocene was added as an internal standard at the end of the experiments. Procedure for the cyclic voltammetry experiment: 0.05 mmol of **1**–**4** was dissolved in 10 mL dry acetonitrile, containing 349.1 mg (1 mmol) of tetrabutylammonium-perchlorate, which served as supporting electrolyte. The solution was bubbled with argon to remove dissolved gas residuals and to ensure inert atmosphere during measurements. The working electrode was wet polished on 0.5 µm

alumina slurry or emery paper grade 500, after each measurement. Cyclic voltammograms were recorded with a scan rate of 100 mV s^{-1}.

3.4. Generation of Diiron-Peroxo Complexes (**5**–**8**)

Precursor complexes (**1**–**4**) were dissolved in 1.5 mL acetonitrile and added 4 equivalent H_2O_2, in different temperature (0, 5, 10 15 °C) and the reactions were followed with UV-Vis spectroscopy at 680 nm, the cuvette length was 1 cm.

3.5. Diiron-Peroxo-Mediated Disproportionaton of H_2O_2

Reactions were carried out by mixing the substrate (H_2O_2) with the in situ generated complex **5**–**8** (1 mM) in 1.5 mL acetonitrile in different temperature (0, 5, 10 15 °C) and the reactions were followed with UV-Vis spectroscopy at 680 nm, the cuvette length was 1 cm. To ensure the reliability of the measurements, 2–3 parallel measurements were performed.

Catalytic reactions were carried out at 20 °C in a 30 cm^3 reactor containing stirring bar under air. In a typical experiment the complex was dissolved dissolved in 20 cm^3 CH_3CN, and the flask was closed with a rubber septum. H_2O_2 was injected by syringe through the septum. The reactor was connected to a graduated burette filled with oil, and the evolved dioxygen was measured volumetrically at time intervals of 2 s.

4. Conclusions

In summary, the results of the reaction kinetics and CV measurements are shown in Table 4. Based on these data the following reaction mechanism, including the diiron-peroxo complex formation, and its reaction with H_2O_2, was proposed (Scheme 3). We obtained clear evidence for the role of the peroxo-intermediate in diiron catalase mimics. We also found that the higher the redox potentials of the Fe^{III}/Fe^{II} redox couple, the higher the catalase-like activity, and the complexes with electron-deficient metal sites are significantly more reactive. It can be explained by their electrophilic character. The results obtained may contribute to the elucidation of the mechanism of both dimanganase and diiron-containing catalase enzymes.

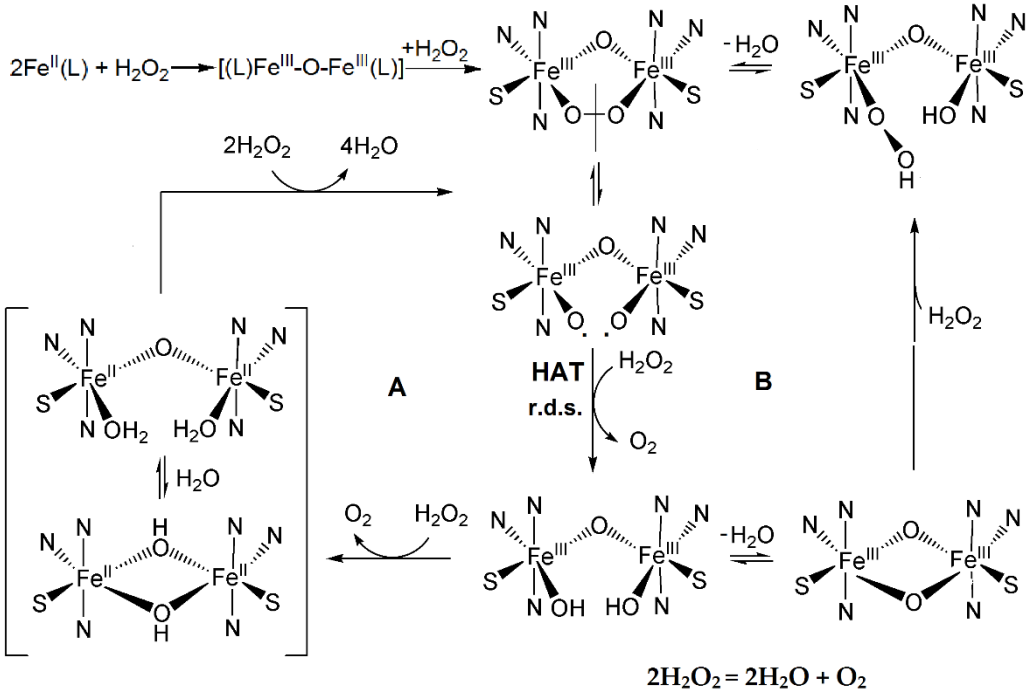

Scheme 3. Proposed mechanism for the formation of $Fe^{III}{}_2(\mu\text{-}O)(\mu\text{-}1,2\text{-}O_2)(L_1\text{-}L_4)_2(Solv)_2]^{2+}$ (**5**–**8**) complexes and their catalase-like reactions.

Author Contributions: Conceptualization, J.K.; resources, D.L.-B., P.T., F.V.C., S.K. and B.G., writing—original draft preparation, J.K., writing—review and editing, J.K. All authors have read and agreed to the published version of the manuscript.

Funding: Financial support of the GINOP-2.3.2-15-2016-00049 (J.K.) and TKP2020-IKA-07 (J.K. and D.L.-B.) are gratefully acknowledged.

Institutional Review Board Statement: Not applicable.

Informed Consent Statement: Not applicable.

Data Availability Statement: Not available.

Conflicts of Interest: The authors declare no conflict of interest.

Sample Availability: Not available.

References

1. Beyer, W.F.; Fridovich, I. Catalases-with and without heme. *Basic Life Sci.* **1988**, *49*, 651–661. [PubMed]
2. Nicholls, P.; Fita, I.; Loewen, P.C. Enzymology and structure of catalases. *Adv. Inorg. Chem.* **2001**, *51*, 51–106. [CrossRef]
3. Kono, Y.; Fridovich, I. Isolation and characterization of the pseudocatalase of *Lactobacillus plantarum*. *J. Biol. Chem.* **1983**, *258*, 6015–6019. [CrossRef]
4. Barynin, V.V.; Whittaker, M.M.; Antonyuk, S.V.; Lamzin, V.S.; Harrison, P.M.; Artymiuk, P.J.; Whittaker, J.W. Crystal Structure of Manganese Catalase from *Lactobacillus plantarum*. *Structure* **2001**, *9*, 725–738. [CrossRef]
5. Antonyuk, S.V.; Melik-Adman, V.R.; Popov, A.N.; Lamzin, V.S.; Hempstead, P.D.; Harrison, P.M.; Artymyuk, P.J.; Barynin, V.V. Three-dimensional structure of the enzyme dimanganese catalase from *Thermus thermophilus* at 1 Å resolution. *Crystallogr. Rep.* **2000**, *45*, 105–113. [CrossRef]
6. Barynin, V.V.; Grebenko, A.I. T-catalase is nonheme catalase of the extremely thermophilic bacterium *Thermus thermophilus* HB8. *Dokl. Akad. Nauk SSSR* **1986**, *286*, 461–464.
7. Allgood, G.S.; Perry, J.J. Characterization of a manganese-containing catalase from the obligate thermophile *Thermoleophilum album*. *J. Bacteriol.* **1986**, *168*, 563–567. [CrossRef] [PubMed]
8. Amo, T.; Atomi, H.; Imanaka, T. Unique Presence of a Manganese Catalase in a Hyperthermophilic Archaeon, *Pyrobaculum calidifontis* VA1. *J. Bacteriol.* **2002**, *184*, 3305–3312. [CrossRef] [PubMed]
9. Whittaker, J.W. Non-heme manganese catalase-the "other" catalase. *Arch. Biochem. Biophys.* **2012**, *525*, 111–120. [CrossRef]
10. Cardenas, J.P.; Quatrini, R.; Holmes, D.S. Aerobic Lineage of the Oxidative Stress Response Protein Rubrerythrin Emerged in an Ancient Microaerobic, (Hyper)Thermophilic Environment. *Front. Microbiol.* **2016**, *7*, 1822–1831. [CrossRef] [PubMed]
11. Bihani, S.C.; Chakravarty, D.; Ballal, A. KatB, a cyanobacterial Mn-catalase with unique active site configuration: Implications for enzyme function. *Free Radic. Biol. Med.* **2016**, *93*, 118–129. [CrossRef]
12. Signorella, S.; Palopoli, C.; Ledesma, G. Rationally designed mimics of antioxidant manganoenzymes: Role of structural features in the quest for catalysts with catalaseand superoxide dismutase activity. *Coord. Chem. Rev.* **2018**, *365*, 75–102. [CrossRef]
13. Wu, A.J.; Penner-Hahn, J.E.; Pecoraro, V.L. Structural, Spectroscopic, and Reactivity Models for the Manganese Catalases. *Chem. Rev.* **2004**, *104*, 903–938. [CrossRef] [PubMed]
14. Tovmasyan, A.; Maia, C.G.C.; Weitner, T.; Carballal, S.; Sampaio, R.S.; Lieb, D.; Ghazaryan, R.; Ivanovic-Burmazovic, I.; Radi, R.; Reboucas, J.S.; et al. A comprehensive evaluation of catalase-like activity of different classes of redox-active therapeutics. *Free Radic. Biol. Med.* **2015**, *86*, 308–321. [CrossRef] [PubMed]
15. Batinic-Haberle, I.; Tovmasyan, A.; Spasojevic, I. An educational overview of the chemistry, biochemistry and therapeutic aspects of Mn porphyrins—From superoxide dismutation to HO-driven pathways. *Redox Biol.* **2015**, *5*, 43–65. [CrossRef]
16. Kaizer, J.; Baráth, G.; Speier, G.; Réglier, M.; Giorgi, M. Synthesis, structure and catalase mimics of novel homoleptic manganese(II) complexes of 1,3-bis(2′-pyridylimino)isoindoline, Mn(4R-ind)2 (R = H, Me). *Inorg. Chem. Commun.* **2007**, *10*, 292–294. [CrossRef]
17. Kaizer, J.; Kripli, B.; Speier, G.; Párkányi, L. Synthesis, structure, and catalase-like activity of a novel manganese(II) complex: Dichloro[1,3-bis(2′-benzimidazolylimino)isoindoline]manganese(II). *Polyhedron* **2009**, *28*, 933–936. [CrossRef]
18. Kaizer, J.; Csay, T.; Kővári, P.; Speier, G.; Párkányi, L. Catalase mimics of a manganese(II) complex: The effect of axial ligands and pH. *J. Mol. Catal. A Chem.* **2008**, *280*, 203–209. [CrossRef]
19. Kripli, B.; Garda, Z.; Sólyom, B.; Tircsó, G.; Kaizer, J. Formation, stability and catalase-like activity of mononuclear manganese(II) and oxomanganese(IV) complexes in protic and aprotic solvents. *NJC* **2020**. [CrossRef]
20. Stadtman, E.R.; Berlett, B.S.; Chock, P.B. Manganese-dependent disproportionation of hydrogen peroxide in bicarbonate buffer. *Proc. Natl. Acad. Sci. USA* **1990**, *87*, 384–388. [CrossRef]
21. Kripli, B.; Sólyom, B.; Speier, G.; Kaizer, J. Stability and Catalase-Like Activity of a Mononuclear Non-Heme Oxoiron(IV) Complex in Aqueous Solution. *Molecules* **2019**, *24*, 3236. [CrossRef]
22. Szávuly, M.I.; Surducan, M.; Nagy, E.; Surányi, M.; Speier, G.; Silaghi-Dumitrescu, R.; Kaizer, J. Functional models of nonheme enzymes: Kinetic and computational evidence for the formation of oxoiron(IV) species from peroxo-diiron(III) complexes, and their reactivity towards phenols and H_2O_2. *Dalton Trans.* **2016**, *45*, 14709–14718. [CrossRef] [PubMed]

23. Pap, J.S.; Draksharapu, A.; Giorgi, M.; Browne, W.R.; Kaizer, J.; Speier, G. Stabilisation of mu-peroxido-bridged Fe(III) intermediates with non-symmetric bidentate N-donor ligands. *Chem. Commun.* **2014**, *50*, 1326–1329. [CrossRef] [PubMed]
24. Pap, J.S.; Cranswick, M.A.; Balogh-Hergovich, É.; Baráth, G.; Giorgi, M.; Rohde, G.T.; Kaizer, J.; Speier, G.; Que, L., Jr. An Iron(II)[1,3-bis(2′-pyridylimino)isoindoline] Complex as a Catalyst for Substrate Oxidation with H_2O_2—Evidence for a Transient Peroxidodiiron(III) Species. *Eur. J. Inorg. Chem.* **2013**, 3858–3866. [CrossRef]
25. Kripli, B.; Csendes, F.V.; Török, P.; Speier, G.; Kaizer, J. Stoichiometric Aldehyde Deformylation Mediated by Nucleophilic Peroxo-diiron(III) Complex as a Functional Model of Aldehyde Deformylating Oxygenase. *Chem. Eur. J.* **2019**, *25*, 14290–14294. [CrossRef]
26. Török, P.; Unjaroen, D.; Csendes, F.V.; Giorgi, M.; Browne, W.R.; Kaizer, J. A nonheme peroxo-diiron(III) complex exhibiting both nucleophilic and electrophilic oxidation of organic substrates. *Dalton Trans.* **2021**, *50*, 7181–7185. [CrossRef] [PubMed]
27. Kripli, B.; Szávuly, M.; Csendes, F.V.; Kaizer, J. Functional models of nonheme diiron enzymes: Reactivity of the mu-oxo-mu-1,2-peroxo-diiron(III) intermediate in electrophilic and nucleophilic reactions. *Dalton Trans.* **2020**, *49*, 1742–1746. [CrossRef] [PubMed]
28. Oloo, W.N.; Fielding, A.J.; Que, L., Jr. Rate determining water assisted O-O bond cleavage of a FeIII-OOH intermediate in a bioinspired nonheme iron-catalyzed oxidation. *J. Am. Chem. Soc.* **2013**, *135*, 6438–6441. [CrossRef]
29. Meena, B.I.; Kaizer, J. Design and Fine-Tuning Redox Potentials of Manganese(II) Complexes with Ioindoline-Based Ligands: H_2O_2 Oxidation and Oxidative Bleaching Performance in Aqueous Solution. *Catalysts* **2020**, *10*, 404. [CrossRef]
30. Jensen, M.P.; Payeras, A.M.I.; Fiedler, A.T.; Costas, M.; Kaizer, J.; Stubna, A.; Münck, E.; Que, L., Jr. Kinetic Analysis of the Conversion of Nonheme (Alkylperoxo)iron(III) Species to Iron(IV) Complexes. *Inorg. Chem.* **2007**, *46*, 2398–2408. [CrossRef]
31. Csonka, R.; Speier, G.; Kaizer, J. Isoindoline-derived ligands and applications. *RSC Adv.* **2015**, *5*, 18401–18419. [CrossRef]